

ChemComm

Accepted Manuscript



This is an *Accepted Manuscript*, which has been through the Royal Society of Chemistry peer review process and has been accepted for publication.

Accepted Manuscripts are published online shortly after acceptance, before technical editing, formatting and proof reading. Using this free service, authors can make their results available to the community, in citable form, before we publish the edited article. We will replace this *Accepted Manuscript* with the edited and formatted *Advance Article* as soon as it is available.

You can find more information about *Accepted Manuscripts* in the [Information for Authors](#).

Please note that technical editing may introduce minor changes to the text and/or graphics, which may alter content. The journal's standard [Terms & Conditions](#) and the [Ethical guidelines](#) still apply. In no event shall the Royal Society of Chemistry be held responsible for any errors or omissions in this *Accepted Manuscript* or any consequences arising from the use of any information it contains.

COMMUNICATION

Magnetic nanosensors optimized for rapid and reversible self-assembly

Cite this: DOI: 10.1039/x0xx00000x

Elisenda Rodriguez^a, Victor S. Lelyveld^a, Tatjana Atanasijevic^a, Satoshi Okada^a, and Alan Jasanoff^{a*}

Received 00th January 2012,
Accepted 00th January 2012

DOI: 10.1039/x0xx00000x

www.rsc.org/

Magnetic nanoparticle-based sensors for MRI have been accelerated to a timescale of seconds using densely-functionalized particles of small size. Parameters that increase response rates also result in large nuclear magnetic relaxation rate and light scattering changes, allowing signals to be detected almost immediately after changes in calcium concentration.

Nanoscale biosensors are frequently based on the spatial reorganization of nanoparticle conjugates, which can give rise to a variety of optical or magnetic effects. Magnetic sensors involve magnetic nanoparticles (MNPs), which strongly affect the transverse relaxation time (T_2) of water proton spins detected by nuclear magnetic resonance (NMR) spectroscopy or imaging (MRI). MNP conjugates have been engineered to undergo reversible analyte-dependent aggregation,^{1,2} where the analyte either reversibly cross-links particles itself or modulates binding between moieties attached to the nanoparticle surfaces. This mechanism has yielded sensors capable of producing R_2 ($= 1/T_2$) changes of up to two or threefold.³ Such changes can be detected at nanoparticle concentrations below 100 μM Fe, making MNP-based sensors an attractive alternative to MRI sensors based on T_1 relaxation or other mechanisms. To date, MNP probes that undergo analyte-dependent assembly have been applied for a variety of *in vitro* NMR assays⁴ and as components of implanted biosensors for *in vivo* imaging.⁵

A serious but previously unaddressed limitation of MNP clustering-based sensors is their slow analyte response rates.⁶ Utility of MNP probes is compromised because of the long incubation times required to resolve substantial changes in R_2 and because analyte concentration changes that take place much faster than the sensor response times cannot be detected. R_2 changes initiated by addition of target analytes to MNP aggregation sensors have generally been reported to equilibrate over tens of minutes; this includes MNPs designed to cluster in the presence of glucose,² calcium ions,¹ and proteins.⁷ By comparison, unimolecular sensors detect analytes with response times on the order of seconds or even milliseconds.⁶

How can MNP aggregation kinetics be accelerated? We used the Smoluchowski aggregation-fragmentation formalism to model the dependence of MNP clustering on the characteristics of binary mixtures of particles assumed to interact via complementary surface-

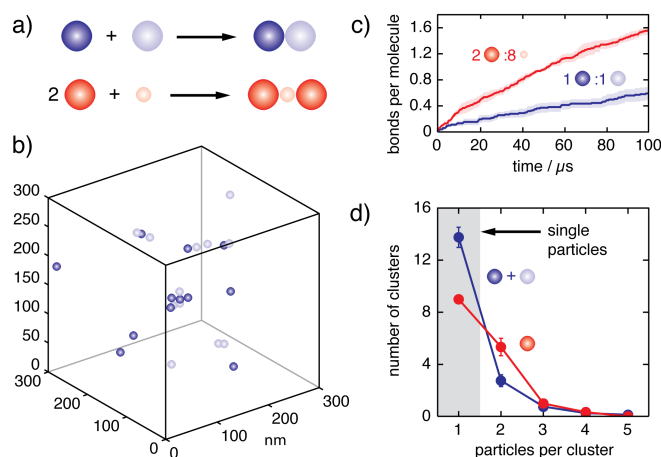


Fig. 1. Increased aggregation rate predicted for asymmetric binary systems. (a) Two scenarios modeled using a Brownian dynamics approach.⁸ In the symmetric scenario, which corresponds to prototypical MNP-based calcium sensors,¹ two types of particle (light vs. dark blue) could combine by contacting each other and forming a bond; bonds could not be formed between particles of the same type. In the asymmetric scenario implemented experimentally in this paper, particles (dark red) could combine only by being bridged by crosslinking domains (light red) with half the diameter of each particle; crosslinking domains could not aggregate on their own. (b) The configuration of 24 particles following 100 μs of simulation in the symmetric interaction scenario in a 300 nm cubic volume with repeating boundary conditions. (c) Mean number of bonds per molecule (particles and crosslinkers included) over time for simulations of symmetric (blue, $n = 8$) and asymmetric (red, $n = 3$) scenarios. Simulations contained equal numbers of particles, with the number of crosslinking domains (light red) in the asymmetric scenario chosen to match the surface area of the particles (dark red). (d) Distribution of cluster sizes following 100 μs simulations depicted in (c). Clusters were classified based on how many particles they contained [light and dark blue or dark red in panel (a)]. The asymmetric scenario (red) produced significantly fewer single-particle species ($p = 0.005$) and more clustered species ($p = 0.0004$) than the symmetric scenario (blue).

conjugated binding domains.⁶ Optimal rates were predicted when the density of surface functionalization moieties was highest for each MNP. Rates were also predicted to increase for constant MNP volume fraction by using smaller particles. Although the minimum size of interacting nanoparticles is restricted by the physical requirements for effective imaging agents, binary aggregating systems can be constructed by pairing MNPs with smaller crosslinking species.² Monte Carlo simulations (Fig. 1) predicted that asymmetric binary systems with similar total particle surface area exhibit roughly twofold faster clustering kinetics than binary systems with two equal particle sizes.

We implemented strategies predicted to enhance MNP sensing kinetics by adapting a prototypical MNP-based calcium ion sensor presented in an earlier study.¹ In this sensor, two different nanoparticle species are prepared separately by conjugation to the calcium-binding protein calmodulin (CaM) and to a peptide (RS20) that binds CaM only in its Ca^{2+} -complexed form. Calcium therefore promotes multivalent binding between complementary particles and reversible clustering with an effective Ca^{2+} dissociation constant of $\sim 1 \mu\text{M}$. CaM and RS20 were incorporated into a new MNP platform with reduced particle size, increased protein surface conjugation density, and an asymmetric binary clustering mechanism.

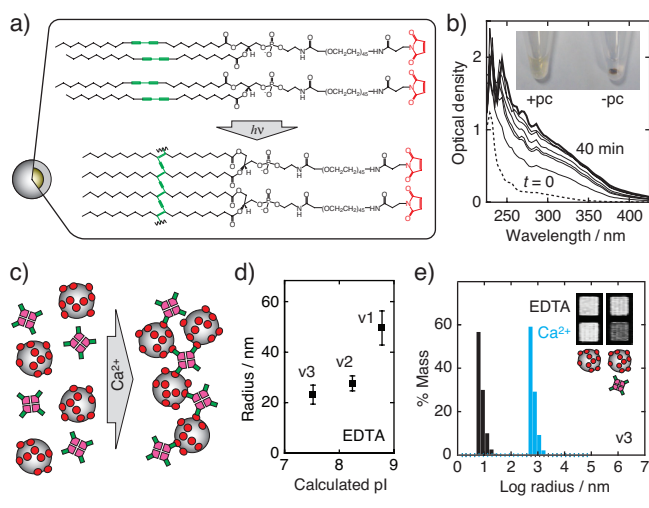


Fig. 2. Optimized nanoparticle aggregation-based sensors. (a) Highly functionalized MNPs are formed by coating iron oxide cores (left) with 23:2 diyne PE-PEG-maleimide. The coating is stabilized by photocrosslinking of the diacetylene moieties (green), which polymerize following irradiation (below arrow). (b) Absorbance spectra taken at time points during irradiation of an MNP sample containing $\sim 1.5 \text{ mM Fe}$; a limiting spectrum (thick line) is approached after 40 minutes. Inset illustrates enhanced stability of photocrosslinked particles (+pc) compared with controls (-pc) in 50% ethanol. The -pc sample is precipitated (brown mark), while the +pc sample remains in suspension. (c) Sensors for Ca^{2+} consist of photocrosslinked particles (pLCIOs, gray) conjugated to CaM (red) and mixed with a smaller partner consisting of the CaM binding domain RS20 (green) fused to DsRed (magenta). (d) DLS radii of sensor mixtures formed in $250 \mu\text{M}$ EDTA, consisting of CaM-conjugated nanoparticles and three DsRed-RS20 mutants (v1-v3) with varying estimated isoelectric point (pI), showing effects of electrostatic tuning on Ca^{2+} -independent aggregation. (e) DLS sizes obtained from optimized sensors with a CaM:RS20 ratio of 1:2 in $250 \mu\text{M}$ EDTA (black) and after addition of $75 \mu\text{M}$ excess CaCl_2 (cyan). Inset: T_2 -weighted MRI scans (spin echo $TE/TR = 150/3125 \text{ ms}$) of samples under Ca^{2+} and EDTA conditions, either with (right) or without (left) addition of DsRed-RS20.v3.

Small, stable, and highly functionalized MNPs were prepared using a novel coating approach (Fig. 2a), based on photocrosslinking of diacetylene-containing lipids.⁹ Oleate-stabilized iron oxide cores were mixed with 1,2-bis(10,12-tricosadiynoyl)-*sn*-glycero-3-phosphoethanolamine-*N*-[maleimide(polyethylene glycol)-2000] (23:2 diyne PE-PEG-maleimide), and transferred to aqueous solvent. The resulting lipid-coated particles were subjected to ultraviolet (UV) irradiation at 254 nm for 40 minutes. Progress of the reaction was indicated by UV-visible spectroscopy (Fig. 2b), and the resulting photocrosslinked lipid-coated iron oxide (pLCIO) nanoparticles were purified by ultracentrifugation to remove micelles and empty liposomes. Particles were characterized by transmission electron microscopy, which indicated electron dense core diameters of 5-10 nm, and by DLS, which indicated a total particle diameter of $16 \pm 3 \text{ nm}$ (Fig. S1), considerably smaller than commonly used dextran-coated superparamagnetic particles. Enhanced stability of the pLCIO particles vs. uncrosslinked particles was confirmed by comparing their resistance to liposome-disrupting conditions¹⁰ (Fig. 2b, inset), as well as functional tests of calcium sensing properties; these tests revealed that sensors formed from uncrosslinked lipid-coated particles¹¹ were susceptible to apparent degradation by metal chelators and to spontaneous calcium-independent dissociation of clusters (Fig. S2).

The pLCIOs were conjugated to CaM via a site-specifically incorporated N-terminal cysteine residue. Protein quantification showed that up to $0.13 \mu\text{M}$ CaM per $1 \mu\text{M}$ iron could be conjugated via thiol-maleimide chemistry. This suggests, together with the particle dimensions, that stoichiometries in the range of 10^2 - 10^3 CaM moieties per pLCIO particle are attainable, corresponding to functionalization density on the order of one molecule/ nm^2 , due to the fact that every lipid terminates in a potential conjugation site. MRI assessment of CaM conjugated pLCIOs indicated a transverse relaxivity of $47 \pm 4 \text{ (mM Fe)}^{-1}\text{s}^{-1}$, measured at 4.7 T.

Asymmetric binary calcium sensors were assembled by pairing CaM-pLCIOs with a polyvalent engineered protein binding partner, rather than a second nanoparticle species (Fig. 2c). The binding partner was formed by fusing an enhanced version of the 28 kD fluorescent protein DsRed¹² to the N-terminus of RS20 (Fig. 2c). DsRed forms obligate tetramers with a diameter of approximately 6 nm.¹³ DsRed-RS20 proteins displayed calcium-dependent clustering in combination with CaM-pLCIOs, but the aggregation was difficult to reverse except at elevated ionic strength, suggesting that dissociation was hindered by calcium-independent electrostatic interactions. To address this problem, we introduced charge reversal mutations in the DsRed-RS20 construct (Fig. S3) and evaluated reversibility of the corresponding sensors formed by mixing with CaM-pLCIOs. Sensor properties were progressively improved by mutations K249E, targeting a linker residue between the DsRed and RS20 moieties, and by K188E, at a superficial solvent-exposed residue on DsRed (Fig. 2d). A variant with both substitutions, DsRed-RS20.v3, was used for all further experiments.

Sensors formed from CaM-pLCIOs and DsRed-RS20.v3 were characterized by DLS and MRI. Sensors initially in EDTA responded to addition of excess CaCl_2 by forming clusters ~ 100 times larger than observed in EDTA (Fig. 2e). Increases in size coincided with decreases in T_2 -weighted MRI signal in the presence of the DsRed-RS20 species (Fig. 2e, inset).

Multiple cycles of clustering and de-clustering were observed by DLS upon successive additions of excess CaCl_2 and EDTA (Fig. 3a). In each case, substantial size changes were apparent in seconds for aggregation at high $[\text{Ca}^{2+}]$ and within the $\sim 3 \text{ s}$ mixing dead time following EDTA addition for disaggregation at low $[\text{Ca}^{2+}]$ (Fig. 3a). The effective rate constant for clustering was $0.252 \pm 0.004 \text{ min}^{-1}$ for sensors containing $50 \mu\text{M Fe}$, $12.5 \mu\text{M DsRed-RS20.v3}$, and 3.75

μM CaM at 37 °C (Figure S4). We determined a midpoint for calcium responsiveness (EC_{50}) $\sim 1 \mu\text{M}$ Ca^{2+} for this sensor at steady state, which makes it applicable for the detection of biologically-relevant calcium fluctuations (Fig. S5). The dynamics of sensor clustering varied systematically as a function of CaM levels conjugated to CaM-pcLCIOs (0.006-0.13 μM CaM per μM Fe), with higher levels of CaM per particle resulting in faster and more pro-

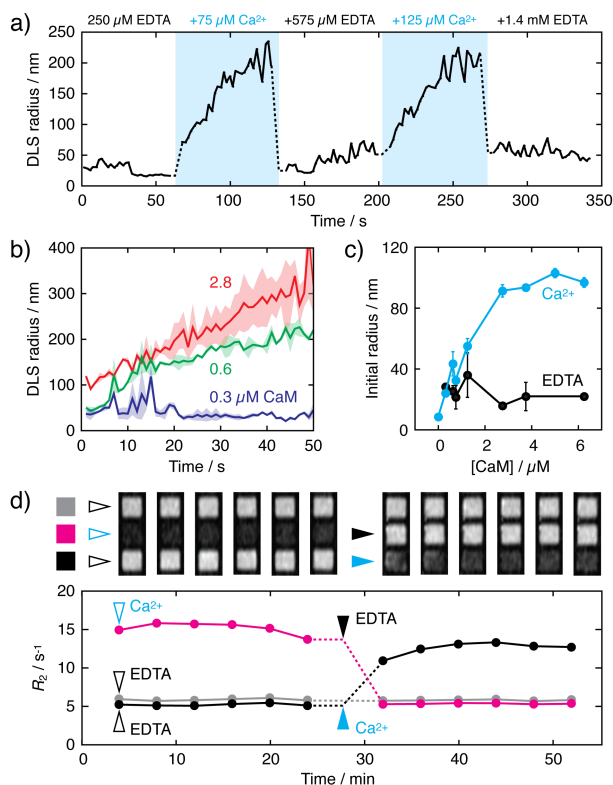


Fig. 3. MNP sensor kinetics. (a) Particle radii as a function of time over two cycles of excess calcium addition and chelation to sensors that contained 50 μM Fe, 1.3 μM CaM, and 12.5 μM DsRed-RS20.v3. Blue indicates periods of high free $[\text{Ca}^{2+}]$, and concentrations of excess Ca^{2+} or EDTA present at each time block are indicated. (b) Particle aggregation after 75 μM excess CaCl_2 addition is a function of the level of CaM conjugated to the particle surfaces for sensors initially in 250 μM EDTA. Samples each contained 12.5 μM DsRed-RS20.v3 and MNP concentrations corresponding to 50 μM Fe conjugated to 0.3 (dark blue), 0.6 (green), or 2.8 μM (red) CaM. Both initial and final DLS sizes are greater for higher CaM densities. Means (lines) and s.e.m. (shading) for $n = 2$ are shown. (c) The size of aggregates immediately after 75 μM excess calcium addition (blue, dead time ~ 3 s) increased as a function of CaM conjugation level for samples with 0.3-6.3 μM CaM per 50 μM Fe. Conditions correspond to panels a-b, and EDTA-only controls are shown in black. Error bars show s.e.m. for $n = 2$. (d) MRI visualizes changes in R_2 (graph below) and T_2 -weighted image intensity (above; spin echo $TE/TR = 160/2000$ ms) within minutes of calcium or EDTA addition. Here, sensors were formed with 75 μM Fe, 4.5 μM conjugated CaM, and 12.5 μM DsRed-RS20.v3, initially in 250 μM EDTA. At time $t = 0$ min, the magenta sample received an addition of 75 μM Ca^{2+} and the black and gray samples were maintained in EDTA; initial time points were obtained under these conditions (open arrows). At $t = 28$ minutes, the magenta sample received 575 μM EDTA, the black sample received 75 μM Ca^{2+} , and the gray sample received no addition.

nounced aggregation (Fig. 3b), as predicted by the modeling studies.⁶ Conjugation density-dependent differences were particularly notable immediately following the mixing dead time, after which clustering was much more pronounced for the most highly functionalized CaM-pcLCIOs (> 10 -fold DLS radius increase) than for the least functionalized.

Sensor response dynamics were also analyzed by MRI in microtiter plates. Figure 3d shows images obtained as a function of time during modulation of free Ca^{2+} concentrations. Calcium or EDTA was added five minutes before the first scan (the dead time for sample mixing and positioning in the scanner). An approximately threefold R_2 change is observable in the initial acquisition. R_2 values remain stable for several scans, and are then reversed again within ~ 5 minutes upon transition from low $[\text{Ca}^{2+}]$ to high $[\text{Ca}^{2+}]$ or *vice versa*. This is more than an order of magnitude faster than R_2 equilibration times previously reported for MNP aggregation sensors. In particular, for prototypical Ca^{2+} sensors¹ formed without regard for the kinetic optimization principles investigated here, R_2 changes required roughly one hour to equilibrate, despite the use of twofold higher iron concentrations than employed for the experiments of Figure 3d (75 μM Fe).

These results show that robust analyte-dependent responses from nanoparticle aggregation-based probes can be detected within experimental dead times of seconds or minutes by DLS or MRI, respectively, indicating that these types of sensors are appropriate for measurements on biologically and chemically-relevant time scales faster than those previously explored. Examples of potential applications include the rapid *in vivo* detection of metabolites such as glucose, which can change by more than 10% within seconds in brain following stimulation¹⁴ or within minutes following food ingestion.¹⁵ *In vitro* diagnostic modalities based on magnetic⁴ or optically-detected¹⁶ nanoparticle aggregation could also be accelerated, allowing measurements to be made at intervals appropriate for rapidly developing clinical conditions such as anaphylaxis or stroke. Finally, although sensors with improved kinetics do not directly address the need for higher affinity detection of some biological targets, we note that accelerating the rate of responses to targets in general confers greater analyte sensitivity, according to mass action principles. The nanosensor design characteristics examined here, in addition to the novel photocrosslinked coating and electrostatic optimization we employed, could therefore find utility in a broad range of applications.

Notes and references

^a Departments of Biological Engineering, Brain & Cognitive Sciences, and Nuclear Science & Engineering
Massachusetts Institute of Technology, 77 Massachusetts Avenue,
Cambridge, Massachusetts 02139, United States.
jasanoff@mit.edu

† Funding Sources

ER was supported with the Beatriu Pinos Fellowship from the Government of Catalonia and SO was supported by an Uehara Memorial Foundation postdoctoral fellowship. Additional support was provided by NIH grants DP2-OD2114, R01-DA28299, R01-NS76462, and an MIT Simons Center seed grant to APJ.

Electronic Supplementary Information (ESI) available: [Supplemental Methods and References Sections and Figures S1, S2, S3, S4, and S5].
See DOI: 10.1039/c000000x/

- 1 T. Atanasijevic, M. Shusteff, P. Fam, A. Jasanoff, *Proc. Natl. Acad. Sci. U S A*, 2006, **103**, 14707-12.
- 2 E. Y. Sun, R. Weissleder, L. Josephson, *Small*, 2006, **2**, 1144-7.
- 3 L. Josephson, J. M. Perez, R. Weissleder, *Angew. Chem. Int. Ed. Engl.*, 2001, **40**, 3204-6.
- 4 H. Shao, C. Min, D. Issadore, M. Liong, T. J. Yoon, R. Weissleder, H. Lee, *Theranostics*, 2012, **2**, 55-65.
- 5 Y. Ling, T. Pong, C. C. Vassiliou, P. L. Huang, M. J. Cima, *Nat. Biotechnol.*, 2011, **29**, 273-7.
- 6 M. G. Shapiro, T. Atanasijevic, H. Faas, G. G. Westmeyer, A. Jasanoff, *Magn. Reson. Imaging*, 2006, **24**, 449-62.
- 7 J. M. Perez, L. Josephson, T. O'Loughlin, D. Hogemann, R. Weissleder, *Nat. Biotechnol.*, 2002, **20**, 816-20.
- 8 Hütter, M. *J Colloid Interface Sci* **2000**, *231*, 337-50.
- 9 D. S. Johnston, S. Sanghera, M. Pons, D. Chapman, *Biochim. Biophys. Acta*, 1980, **602**, 57-69.
- 10 B. M. Shamsai, H. G. Monbouquette, *J. Memb. Sci.*, 1997, **130**, 173-81.
- 11 N. Nitin, L. E. LaConte, O. Zurkiya, X. Hu, G. Bao, *J. Biol. Inorg. Chem.*, 2004, **9**, 706-12.
- 12 R. L. Strack, D. E. Strongin, D. Bhattacharyya, W. Tao, A. Berman, H. E. Broxmeyer, R. J. Keenan, B. S. Glick, *Nat. Methods*, 2008, **5**, 955-7.
- 13 M. A. Wall, M. Socolich, R. Ranganathan, *Nat. Struct. Biol.*, 2000, **7**, 1133-8.
- 14 E. A. Kiyatkin, M. Lenoir, *J. Neurophysiol.*, 2012, **108**, 1669-84.
- 15 T. C. Dunn, R. C. Eastman, J. A. Tamada, *Diabetes Care*, 2004, **27**, 2161-5.
- 16 W. Zhao, M. A. Brook, Y. Li, *Chembiochem*, 2008, **9**, 2363-71.